The Oklahoma–Kansas Mesoscale Convective System of 10–11 June 1985: Precipitation Structure and Single-Doppler Radar Analysis

STEVEN A. RUTLEDGE

Department of Atmospheric Sciences, Oregon State University, Corvallis, Oregon

ROBERT A. HOUZE, JR., AND MICHAEL I. BIGGERSTAFF

Department of Atmospheric Sciences, University of Washington, Seattle, Washington

THOMAS MATEJKA

National Center for Atmospheric Research, Boulder, Colorado

(Manuscript received 3 December 1987, in final form 11 April 1988)

ABSTRACT

The 10–11 June mesoscale convective system observed in Kansas during PRE-STORM is studied using a variety of observations including conventional radar, satellite, and single-Doppler radar. This storm, at maturity, consisted of a strong line of convection trailed by a broad region of stratiform rain. The PRE-STORM Doppler radar observations show that the general airflow pattern is similar to that seen in previously analyzed cases; however, since the Doppler observations were quite extensive in time and space, they permit several details of the airflow to be revealed for the first time.

A rear inflow jet, front-to-rear flow aloft, and a mesoscale updraft and downdraft were all present. The mesoscale downdraft commenced at the top of the slanted rear inflow jet. Sublimation and evaporation of hydrometeors in this flow apparently generated the necessary cooling to drive the mesoscale downdraft circulation. The intensity and slope of the rear inflow jet varied with location in the storm, which apparently led to differences in both the intensity and depth of the mesoscale downdraft. The intrusion of this inflow jet into the rear of storm occurred at quite high levels and was probably responsible for disruption of the continuous oval cloud shield as viewed by satellite.

The front-to-rear flow situated above the rear inflow jet contained mesoscale upward motion. Vertical velocities obtained by the EVAD (Extended Velocity–Azimuth Display) method reveal a strong mesoscale updraft, with speeds approaching 50 cm s^{-1}. Vertically pointing observations indicated that convective-scale updrafts and downdrafts were present within 20 km of the convective line. Convective-scale features were not observed in the remaining portion of the trailing stratiform region.

1. Introduction

During the field phase of PRE-STORM[1], several squall lines with trailing mesoscale regions of stratiform precipitation were observed. This type of squall line system was first identified in middle latitudes by Newton (1950), Fujita (1955), and Pedgley (1962) and in the tropics by Hamilton and Archbold (1945) and Zipser (1969). A particularly well defined example of this type of storm was documented in great detail in the PRE-STORM observational network on 10–11 June 1985 (Cunning 1986).

The airflow in squall lines with trailing stratiform regions has been examined with soundings from special mesoscale networks (e.g., Ogura and Liou 1980; Gamache and Houze 1982, 1985; Houze and Rappaport 1984; Leary and Rappaport 1987). These studies have shown that the basic mesoscale vertical motion pattern in this type of storm is characterized by mean ascent in the region containing the convective line, and mean ascent at upper levels in the trailing stratiform region with mean descent at lower levels in this region. However, special-network soundings do not have the time or space resolution to show details of the mesoscale circulation, nor can they indicate the pattern of convective air motions superimposed on the mesoscale circulation. Consequently, several recent studies of midlatitude squall lines with trailing stratiform regions have emphasized Doppler radar observations (Smull and Houze 1985, 1987a,b; Srivastava et al. 1986; Kessinger et al. 1987). These studies have identified more detailed kinematic features such as the pattern of intense convective updrafts and downdrafts within the

[1] PRE-STORM is an acronym for Oklahoma–Kansas Preliminary Regional Experiment for the Stormscale Operational and Research Meteorology Program-Central Phase.

Corresponding author address: Dr. Steven A. Rutledge, Dept. of Atmospheric Science, Oregon State University, Corvallis, OR 97331-2209.

convective line, weaker convective drafts located aloft to the rear of the line, mesoscale front-to-rear system-relative flow in the mesoscale updraft of the stratiform region, and mesoscale rear-to-front flow in the mesoscale downdraft. The Doppler radar-derived circulation patterns have further provided a basis for calculations of momentum fluxes (Smull and Houze 1987a) and diagnostic modeling of microphysical processes (Rutledge and Houze 1987).

In this paper, we continue the effort to document squall lines with trailing stratiform regions by examining satellite, conventional radar, and Doppler radar data for the 10–11 June PRE-STORM case. Our objective is to describe the 10–11 June storm's mesoscale organization, evolution and circulation by various methods of analysis short of deducing wind fields from dual-Doppler radar data. Although dual-Doppler syntheses can provide much quantitative detail on the three-dimensional wind field over small regions of the storm, many of the basic kinematic features of the storm can be seen over large regions in the single-Doppler radar data. In addition, analysis of single-Doppler radar data can be performed to yield highly accurate information on the structure and magnitude of mesoscale vertical motion patterns in the trailing stratiform region and, using data when the radar was operated in the vertically pointing mode, on the convective-scale variations in the stratiform cloud as well. These results thereby provide a context in which three-dimensional wind fields obtained from dual-Doppler radar data can be interpreted in future work.

2. Network design, radar characteristics, and scanning procedures

The facilities used in PRE-STORM have been described by Cunning (1986). This paper concentrates on data collected in the Kansas portion of the PRE-STORM network with the NCAR (National Center for Atmospheric Research) CP-3 and CP-4 5 cm wavelength Doppler radars (Table 1). Data from several digitized NWS (National Weather Service) WSR-57 10 cm radars are also used in this study. As shown in Fig. 1, the CP-4 radar was located at Cheney State Park, while the CP-3 radar was deployed 60 km to the north-northwest, near Nickerson, Kansas. Two basic scanning procedures were used at these radars during PRE-STORM, depending upon the meteorological situation. In the standard mode, the radars performed continuous dual-Doppler scans, consisting of simultaneous conical scans in a common domain.

When stratiform precipitation was over the radars, either the standard mode was continued or the stratiform scanning procedure was occasionally invoked. The objective of this latter mode was to obtain time–height cross sections of reflectivity and particle fallspeed within the stratiform region associated with mesoscale convective systems. In this mode, one of the Doppler radars was operated at vertical incidence for approximately one hour while the second radar conducted three-dimensional conical scans interspersed with RHI scans (which were occasionally taken over the vertically pointing radar). From the first radar, the presence of convective-scale updraft and downdraft structures can be inferred from the reflectivity and Doppler velocities measured at vertical incidence. From the second radar, mean vertical air motions in the stratiform region ($|w| \geq 0.1$ m s^{-1}) can be determined from the vertical profile of wind divergence derived from the conical scans. The stratiform mode was employed during a 60 min period of the 10–11 June storm.

TABLE 1. Characteristics of the NCAR radars used in PRE-STORM.

Parameter	Radar	
	CP-3	CP-4
Wavelength (cm)	5.45	5.49
Maximum range (km)	135	135
Nyquist velocity (m s^{-1})	15.37	15.24
Peak power (kW)	400	400
Pulse width (μ sec)	1.0	1.0
Pulse repetition frequency (Hz)	1111	1111
Minimum detectable signal (dBm)	−113	−112
Number of range gates	512	512
Azimuthal resolution (deg)	0.8	0.8
Gate spacing (m)	260/150*	260/150*
Number of samples	64/256†	64/256†

* A gate spacing of 150 m was used for the EVAD and vertically pointing scans.

† Number of samples was set at 256 for the vertically pointing mode.

3. Overview of satellite imagery and radar reflectivity patterns

In this section, we present an overview of the storm structure and development as seen in enhanced infrared satellite imagery (Fig. 2) and WSR-57 radar data (Fig. 3). The infrared imagery indicates the areal coverage and structure of the high clouds associated with the storm whereas the WSR-57 data reveals the low-level structure and organization of the precipitation below the cloud tops.

The enhanced infrared satellite imagery at 2300 UTC 10 June (Fig. 2a) showed cold cloud shields (cloud top temperatures < -50°C) over western Kansas in association with the developing convective line and over the Nebraska–Iowa border in association with a dissipating convective system. Remnants of yet another dissipating mesoscale system that affected the PRE-STORM network earlier on 10 June were also present near the Kansas–Missouri border. By 0100 UTC 11 June (subtract 5 h to obtain local Central Daylight Time) the upper-level cloud shield covered much of Kansas (Fig. 2b). Cloud top temperatures < -70°C were apparent along the southern flank, near the location of the most intense convection. By this time,

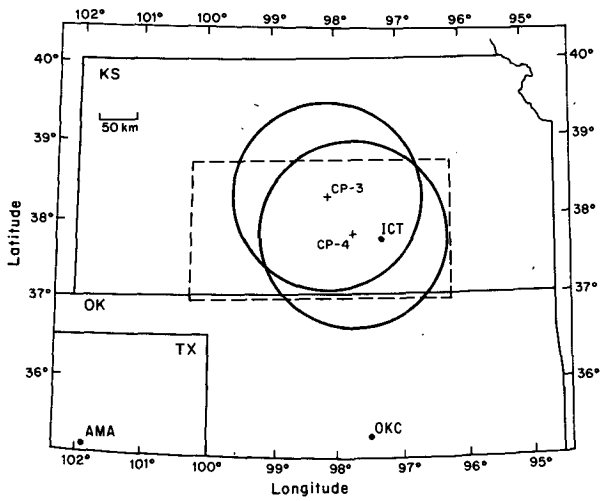

FIG. 1. Map indicating the location of the NCAR 5 cm Doppler radars and their maximum range circles. The Wichita WSR-57 10 cm radar was located at ICT. Detailed surface observations in the Kansas portion of PRE-STORM were obtained within the dashed rectangle. Other 10 cm radars used in this study were located in Oklahoma City, Oklahoma (OKC) and Amarillo, Texas (AMA).

the storm had achieved the size and temperature criteria of a mesoscale convective complex (MCC) as defined by Maddox (1980). Over the time period from 0200–0300 UTC (Figs. 2c, d) the cloud shield continued to expand, and a well-defined inner-core region with temperatures $< -70°C$ covering some 30 000 km^2 had developed. Convective cells were at their peak intensity during this period (intensity is discussed in terms of observed radar reflectivities in individual convective cells).

The area of the inner-core cold region had decreased substantially by 0400 UTC (Fig. 2e) in association with the weakening of the deep convection. By 0600 UTC (Fig. 2f) only a small region $< -70°C$ was present, as nearly all the deep convection had dissipated. Furthermore, a splitting of the upper-level cloud shield was becoming evident by the higher cloud-top temperatures bisecting the storm along a northwest–southeast line in central Kansas. By 0700 UTC (Fig. 2g), the storm had separated into two areas. The portion in Kansas consisted only of stratiform precipitation (see Fig. 3g). By 0800 UTC (Fig. 2h), the continuous upper-level cloud shield was either absent over Kansas or too thin to be detected as a low-temperature area in the infrared imagery.

The NWS radar data are presented in the form of composite low-level reflectivity maps obtained from the digitized WSR-57 radars, including Wichita (ICT), Oklahoma City (OKC), and Amarillo (AMA). Although the first radar echoes observed by the ICT radar were near 2200 UTC, the first composite echo pattern shown is for 2320 UTC on 10 June (Fig. 3a). At this time, intense convection was located to the northwest of Wichita and extended in a line to the northern Texas panhandle. Even though the echo was just coming into radar range, it is apparent that light precipitation was already present behind the convective line, though it may not have been reaching the surface. By 0100 UTC (Fig. 3b), a well-defined convective line extended from central Kansas to the western edge of the Texas panhandle. By this time, just three hours after the first radar echoes were observed at ICT, the system satisfied the size criteria put forth by Maddox (1980) to be classified as an MCC. Numerous cells within the line exceeded 50 dBZ. The portion of the line west of Wichita exhibited a virtually solid core of reflectivity > 50 dBZ for more than 70 km in length. The echo to the rear of the convective line was still weak.

Over the period 0200–0400 UTC (Figs. 3c–e) the convective line reached its maximum intensity and coverage and began to dissipate, as evidenced by the decrease in convective cells over 50 dBZ. A large area of stratiform rain exceeding 25 dBZ was present to the rear of the convective line at 0400 UTC. This feature was not seen at earlier times and therefore suggests an expansion and intensification of the trailing stratiform region, although other factors such as the approach of the storm towards the radar and the large beamwidth of the WSR-57 may be involved. The convective echo defining the squall line had begun to dissipate by 0400 UTC, in agreement with the satellite sequence which at this time showed the decay of the inner core region of extremely cold tops ($< -70°C$).

From 0600 to 0800 UTC (Figs. 3f–h), the echo pattern became disorganized and weakened considerably, simultaneously with the dissolution of the well-defined oval cloud shield (Figs. 2f–h). The rear portion of the stratiform echo exhibited a notch or bow-like structure. As Smull and Houze (1985) suggest, this type of echo pattern is probably associated with intense inflow of dry air into the rear of the storm. A rear inflow jet was indeed present in this case (Smull and Houze 1987b) and will be discussed in some detail in the next section. By 0800 UTC (Fig. 3h), the surface precipitation consisted of two stratiform regions, associated with the two areas of cold cloud tops shown in Fig. 2h, and a remant weak convective line near the Texas–Oklahoma border. The surface precipitation pattern as observed by radar exhibited the same splitting through the center of the storm as was observed in the satellite data. We believe this splitting in the area of the rear echo notch was related to the intrusion of a rear inflow jet. The rear inflow jet will be discussed in subsequent sections. Johnson and Hamilton (1988) also discussed the splitting stratiform area and related it to the rear inflow and surface pressure features.

4. Vertical cross section analysis

In this section we present vertical cross sections of reflectivity and storm relative flow obtained during a 4 h period (≈0100–0500 UTC 11 June 1985). Although more details of the flow will be derived by dual-Doppler synthesis and explained in future articles, the

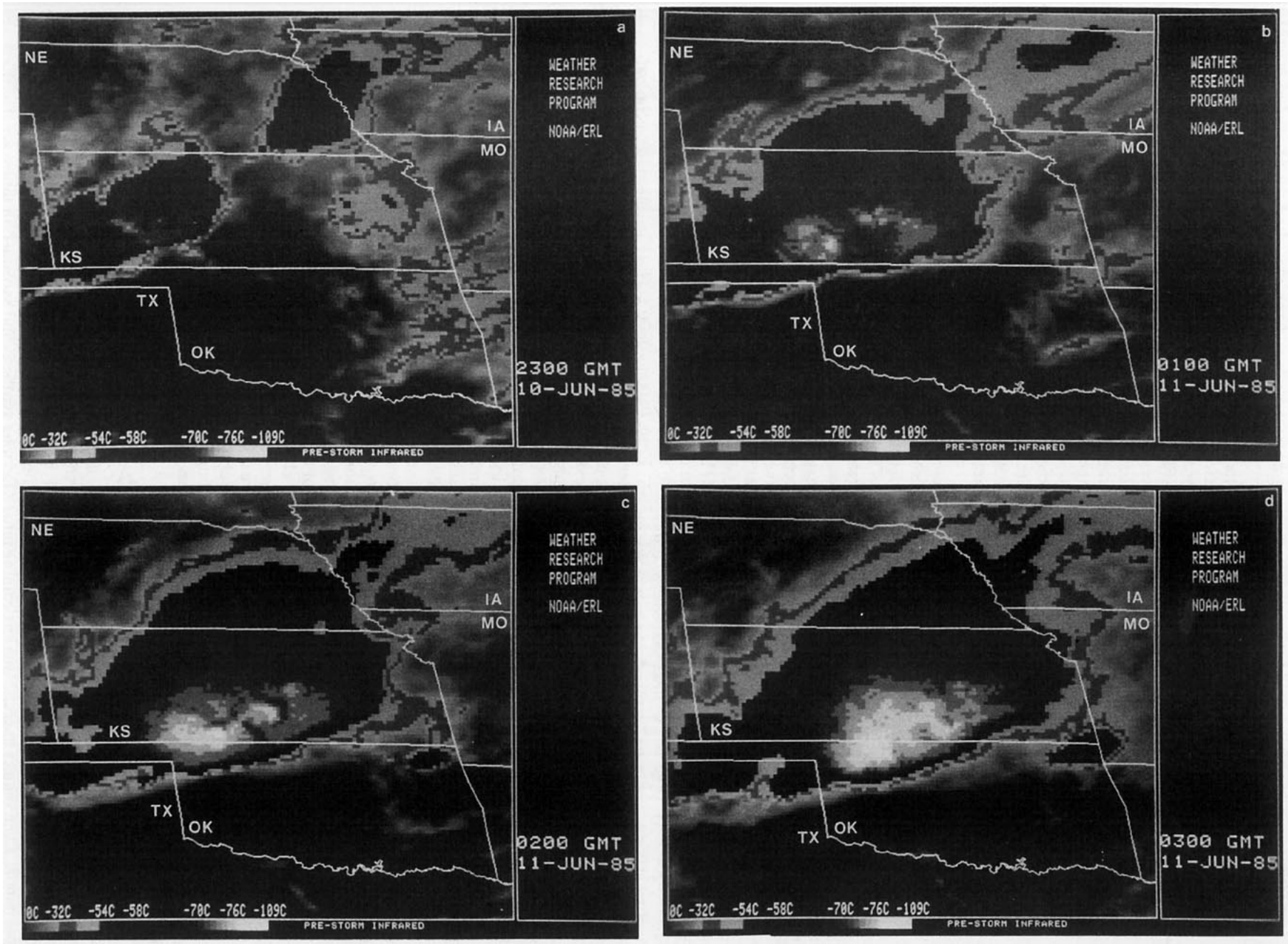

FIG. 2. Enhanced infrared satellite imagery indicating cloud top temperatures for 10–11 June 1985 at (a) 2300 UTC, (b) 0100 UTC, (c) 0200 UTC, (d) 0300 UTC.

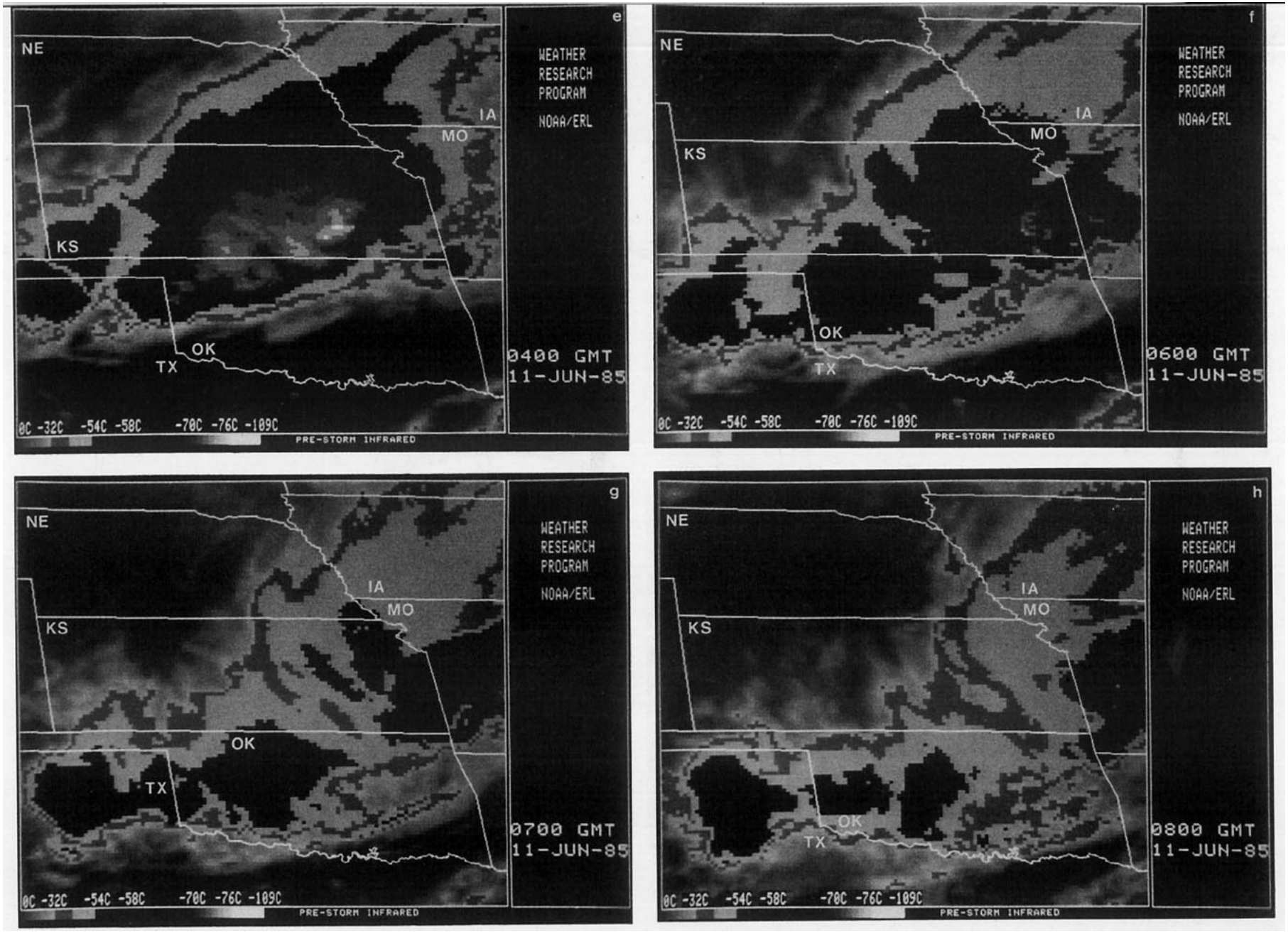

FIG. 2. (*Continued*) (e) 0400 UTC, (f) 0600 UTC, (g) 0700 UTC, and (h) 0800 UTC. Temperature scale (°C) is indicated along the bottom of the figure.

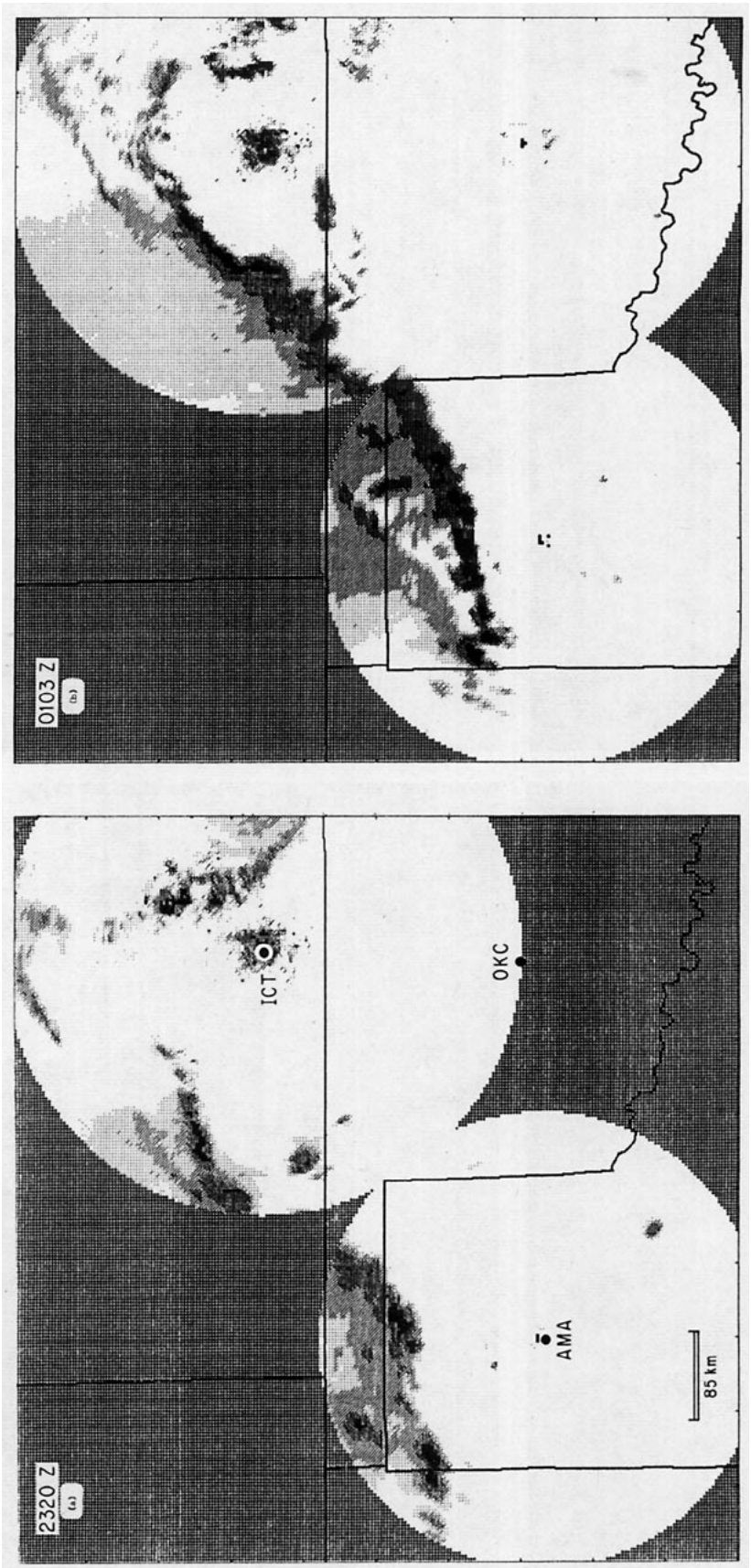

FIG. 3. Composite low-level echo patterns from the AMA, ICT, and OKC WSR-57 10 cm radars for (a) 2320 UTC, (b) 0103 UTC, (c) 0200 UTC, (d) 0300 UTC, (e) 0400 UTC, (f) 0600 UTC, (g) 0700 UTC, and (h) 0800 UTC. The composite echo patterns were formed by merging 1° elevation scans from these radars. Data from each of the three sites were not available at all times. Reflectivity values are 15–25 dBZ, light stippling; 25–35 dBZ, heavy stippling; 35–50 dBZ, hatching; and >50 dBZ, solid. The range circles in (c) and (e) denote coverage of CP-3 and CP-4 and are used as reference for later discussions.

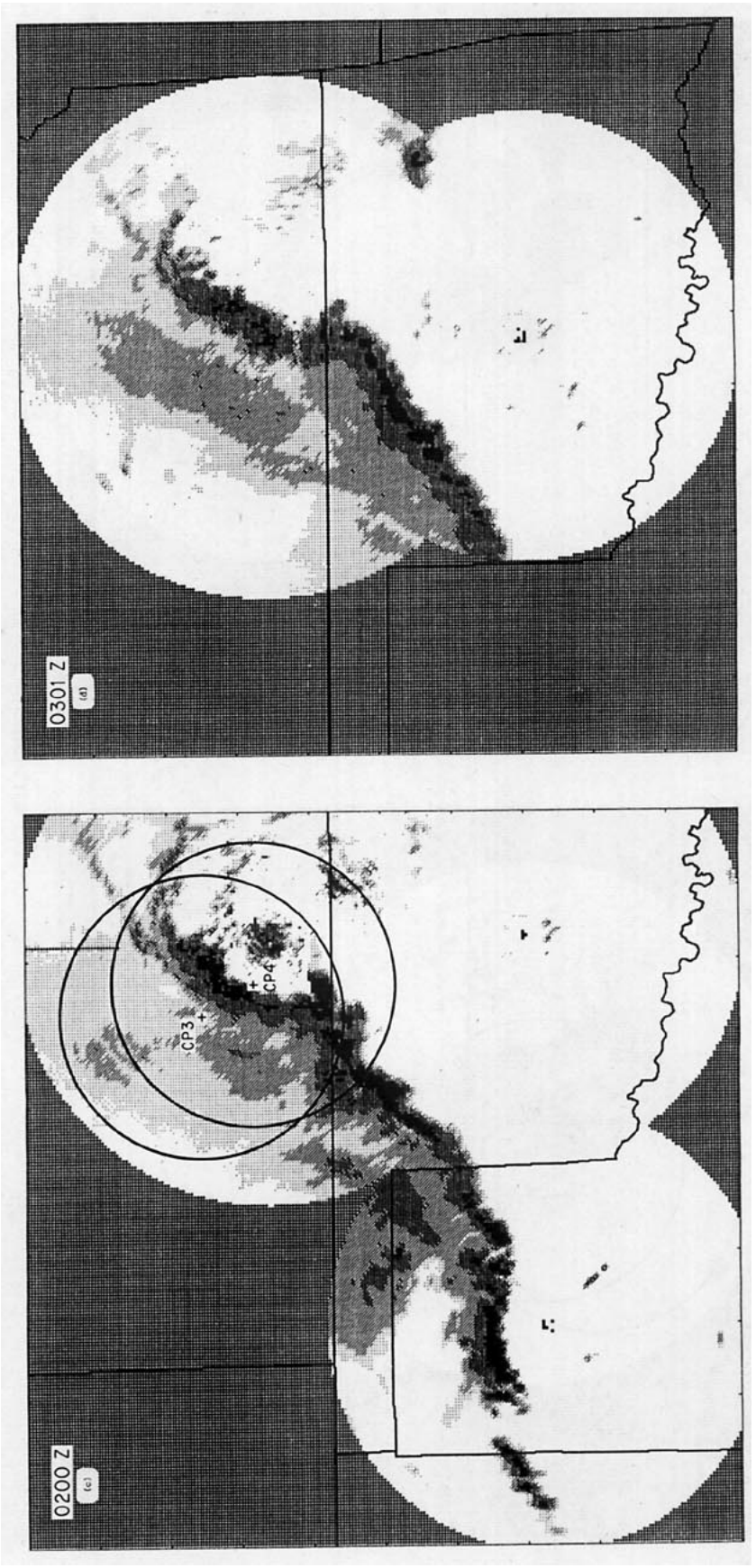

FIG. 3. (*Continued*)

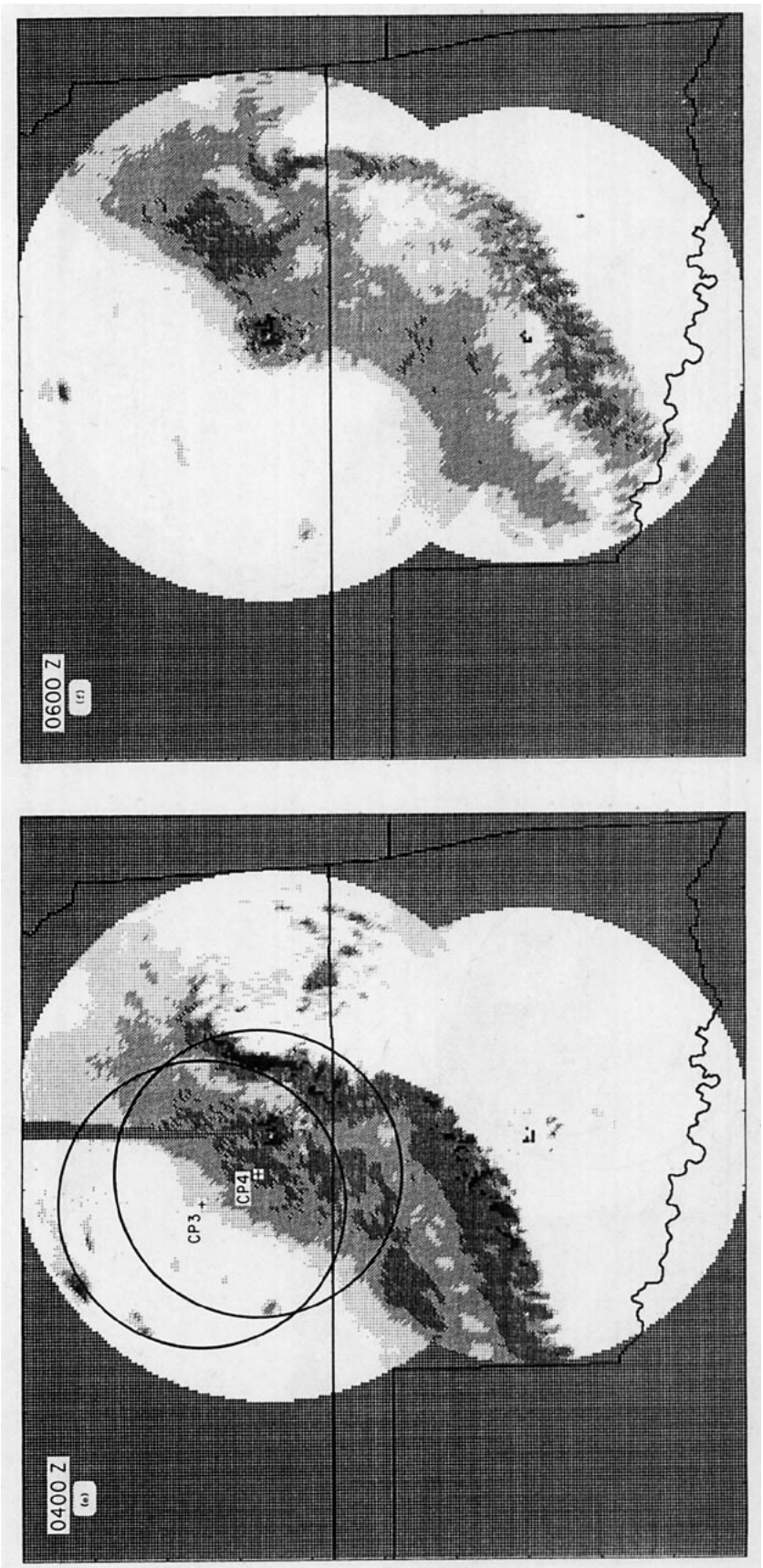

FIG. 3. (*Continued*)

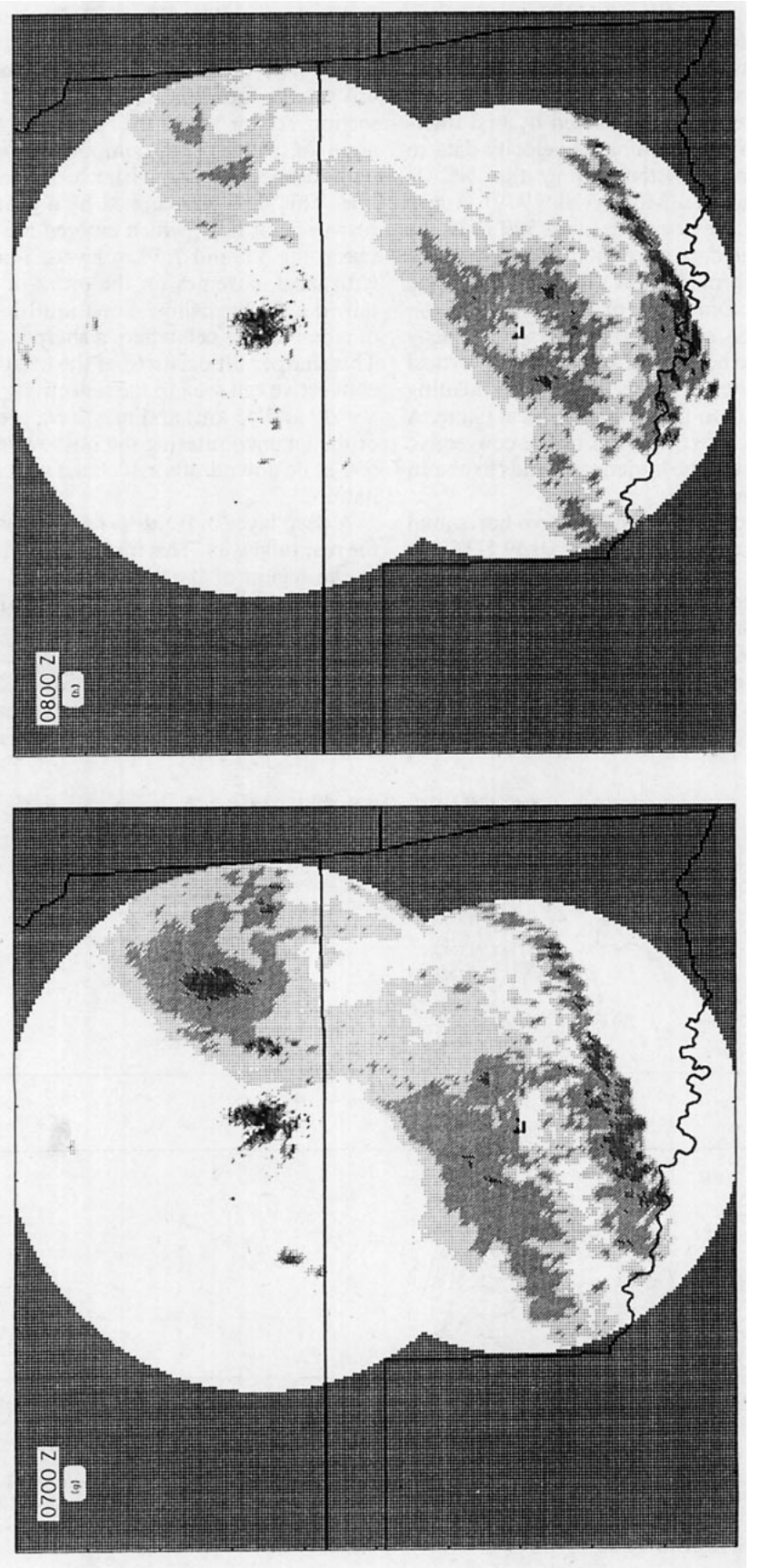

FIG. 3. (*Continued*)

basic mesoscale airflow structure and its changes during this period can be seen by examining these single-Doppler vertical cross sections.

Vertical cross sections oriented in a direction normal to the convective line were constructed by first interpolating the reflectivity and unfolded velocity data to a Cartesian coordinate system using the NCAR SPRINT software package (Mohr et al. 1979). A grid interval of 1.5 km in the horizontal and 500 m in the vertical was used. The data were then shifted in space to account for the storm motion that occurred while the data were taken. Only data obtained at elevation angles < 23° were used, so the measured radial velocity was dominated by the horizontal velocity. The vertical cross sections were then constructed by interpolating the Cartesian grid data to the desired vertical plane. A storm speed of 14 m s^{-1} (the speed of the convective line) was subtracted from the horizontal winds to obtain the storm relative flow.

Cross sections of reflectivity and relative horizontal flow from the CP-4 radar data taken at 0139 UTC are shown in Fig. 4. The positive direction is toward 300° azimuth, while the negative direction is toward 120°. At this time, the storm was approaching CP-4 from the northwest, with the convective line some 40 km from the radar. The cross section intersects a slightly rearward tilting convective echo within the line that has a top approaching 15 km MSL (Fig. 4a). The storm had both a small leading upper-level anvil and a trailing region of light stratiform rain at this time.

The horizontal storm relative velocity pattern (Fig. 4b) reveals four contrasting airflows within the cross section. At low levels, the relative flow had a large negative (or front to rear) component with the layer gradually deepening with distance behind the convective line. This flow was capped by a pronounced layer of rear-to-front flow, which entered the cross section between the 3.5 and 7.5 km levels. This rear inflow jet, with local extremes on the order of 10 m s^{-1}, maintained a fairly shallow slope until it reached the rear of a convective cell where a sharper tilt was observed. This sharper tilt occurred at the location of the intense convective cell seen in the reflectivity pattern (between $x = 30$ and 45 km) and may have been a consequence of the jet encountering the outflow of intense convective-scale downdrafts associated with the heavy precipitation.

A deep layer of front-to-rear flow was located above the rear inflow jet. This front-to-rear flow was enhanced in the region of the convective cell. Rearward acceleration in a line of cumulus convection has been previously documented in a tropical convective line by LeMone (1983) and in another midlatitude squall line (similar to the present case) by Smull and Houze (1985, 1987a). This enhanced rearward flow transports heat, momentum and condensate into the region behind the

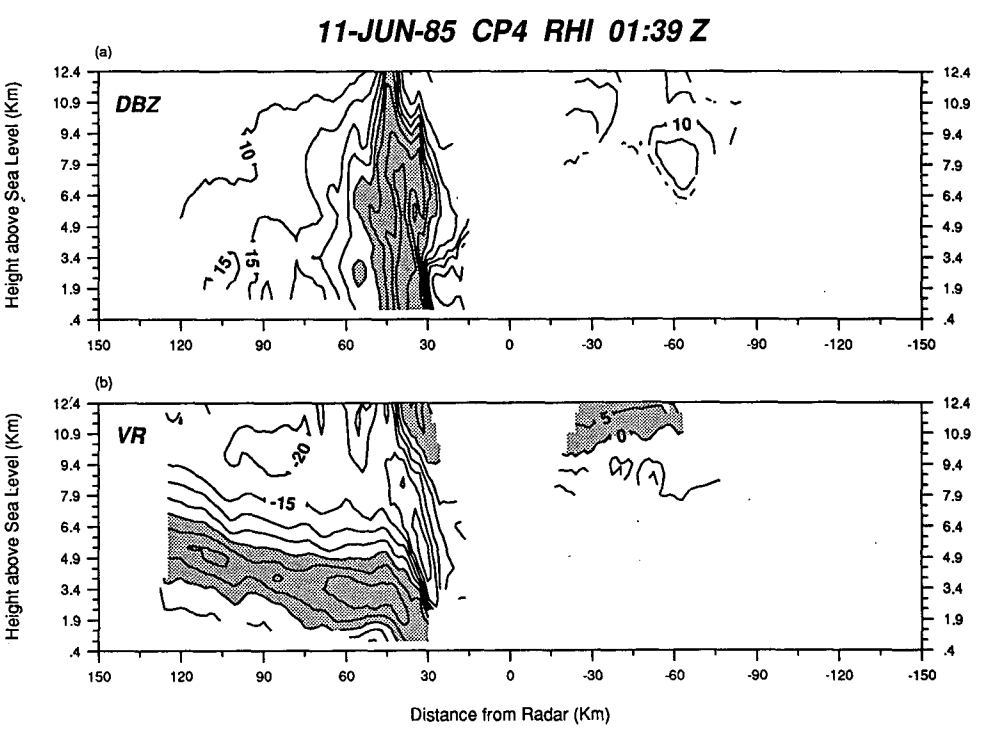

FIG. 4. Vertical cross sections of reflectivity and horizontal flow along 300°–120° radials from CP-4 at 0139 UTC. (a) Reflectivity in dBZ. Contour interval is 5 dBZ. Shading denotes reflectivities > 30 dBZ. (b) Horizontal relative flow in m s^{-1}. Contour interval is 5 m s^{-1}. Shading denotes velocities > 0, or left-to-right motion relative to the storm.

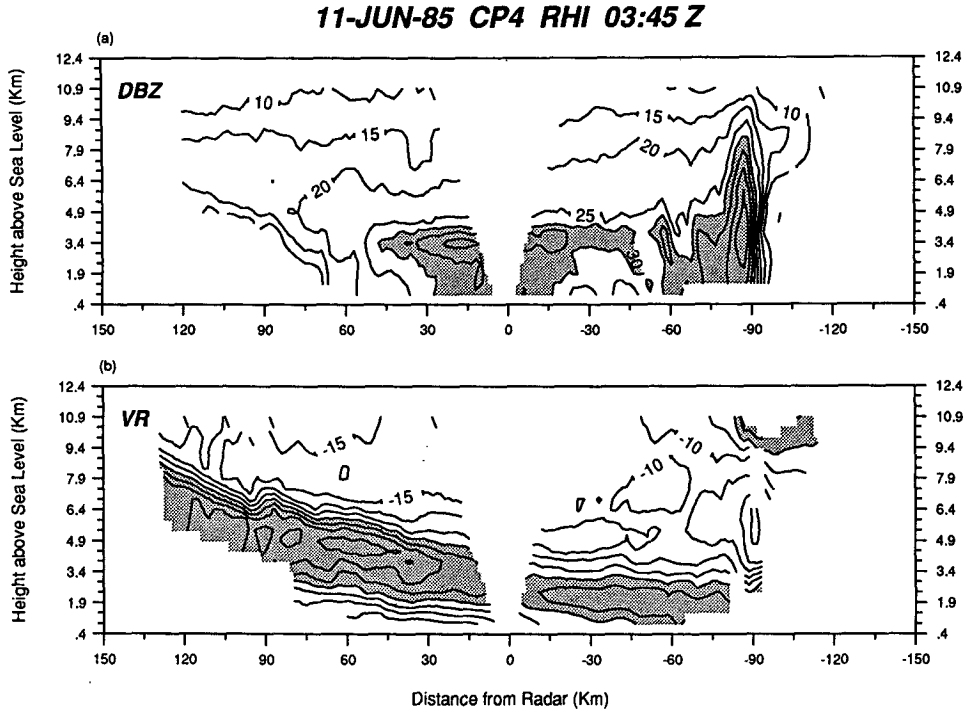

FIG. 5. As in Fig. 4 except for 0345 UTC. (a) Reflectivity in dBZ; (b) horizontal relative flow in m s^{-1}.

convective cells, and thus likely contributes to the genesis and maintenance of the trailing stratiform region. The fourth flow regime in this figure occurs aloft in the leading anvil. In this region the flow is rear-to-front and is driven by intense divergence near the cell top.

Reflectivity and relative velocity cross sections for 0345 UTC from CP-4 are shown in Fig. 5. The orientation is the same as for Fig. 4 (x positive toward 300°, negative toward 120°) and similar to that used in a cross-sectional analysis by Smull and Houze (1987b) in their Fig. 11, which was along azimuths 310° and 130°. This cross section, compared to that in Fig. 4, illustrates the considerable broadening and intensification over time of the surface precipitation associated with the trailing stratiform region indicated by the WSR-57 reflectivity data (section 3). At this time, the stratiform surface precipitation spanned some 130 km in the horizontal, compared to approximately 80 km at 0139 UTC. The broadening of the stratiform precipitation zone is consistent with the continual supply of hydrometeors into this zone from the convective region during the period between 0139 and 0345 UTC and with the development of a well-defined middle to upper tropospheric mesoscale updraft (documented in following sections).

The horizontal flow structure for 0345 UTC (Fig. 5b) again shows the four flow regimes seen in the earlier cross section. However, more information concerning the breadth of these regimes is available in this section. Rear-to-front flow extended throughout the system and entered the rear of the storm at quite high levels. The level of zero relative flow was located near 8.5 km MSL at the rear of the cross section. The entry of the rear inflow at such high levels lends confidence to our inference that this flow was responsible for the disruption of the continuous oval cloud shield seen in the satellite imagery. Local speed maxima exceeded 15 m s^{-1} in the rear portion of the inflow current, but the strength of the rear inflow decreased steadily as it progressed inward toward the convective line. Speeds as low as 5 m s^{-1} were present in the transition zone and rear portion of the convective region.[2]

The strongest front-to-rear flow (< -25 m s^{-1}) was located at the leading portion of the cross section in the immediate vicinity of the convective cell. The front-to-rear current was generally characterized by speeds on the order of -15 m s^{-1}. The front-to-rear flow situated below the rear inflow jet had strengthened considerably since 0139 UTC. A portion of the rear-to-front flow in the leading anvil is evident in the upper right portion of the cross section ($x > 90$ km, $z > 9$ km).

The vertical cross section analysis for 0414 UTC along the 300° and 120° radials from CP-4 is shown in Fig. 6. The reflectivity cross section (Fig. 6a) indicates

[2] As evident in our dual-Doppler analysis of this storm (results to be discussed in later articles), the rear inflow within this region turned to become more parallel to the convective line. Hence the component in the plane of the vertical cross section decreased, explaining the observed decrease seen in Fig. 5b.

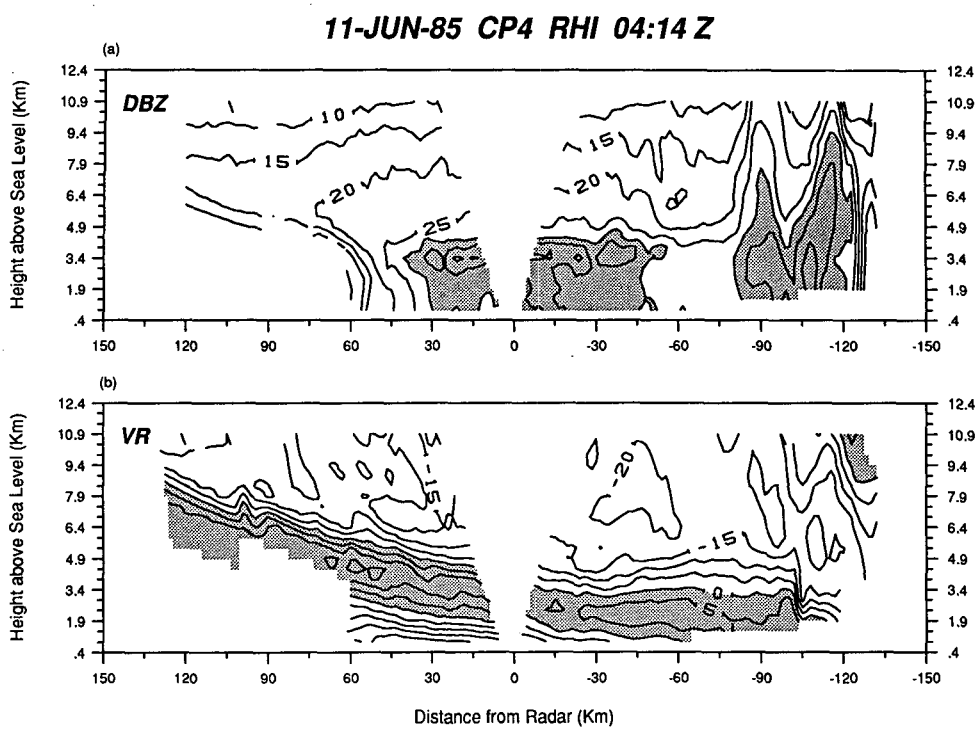

FIG. 6. As in Fig. 4 except for 0414 UTC. (a) Reflectivity in dBZ; (b) horizontal relative flow in m s^{-1}.

the further development of the stratiform surface precipitation, which was near its maximum width and intensity at this time. The radar echo associated with the trailing stratiform region extended well beyond the surface rainfall area, as evident from the anvil-like reflectivity pattern. Apparently, evaporation into the rear inflow was large enough to prevent any precipitation from reaching the surface. This evaporation caused by the rear inflow was probably important in limiting the width of the trailing stratiform surface precipitation. The rear inflow appears to have carved the observed anvil structure from a fairly homogeneous reflectivity feature aloft (note the 10, 15, and 20 dBZ contours in Fig. 6a), suggesting that the surface precipitation would have obtained larger widths had it not been affected by the rear inflow.

The horizontal flow structure is fairly similar to that shown for 0345 UTC; however, some important differences are seen at 0414 UTC. The front-to-rear flow below the rear inflow jet was somewhat stronger than it was at 0345 UTC, with local maxima exceeding 20 m s^{-1} compared to 15 m s^{-1}. This flow increased in speed toward the rear of the stratiform region probably in concert with the development of a wake low pressure region situated at the back edge of the stratiform surface precipitation region (Johnson and Hamilton 1988). Wake lows are typically seen at the rear edge of the stratiform rain region (Fujita 1955; Pedgley 1962; Zipser 1977; Smull and Houze 1985). The front-to-rear flow aloft was also considerably stronger at this time than at 0345 UTC. Areas of velocities > 20 m s^{-1} were found over considerable expanses in this flow.

Figure 7 shows the reflectivity and horizontal velocity vertical cross sections from CP-3 at 0414 UTC, along the 300°–120° radials. (The cross sections presented in Figs. 6 and 7 represent two planes perpendicular to the squall line separated by approximately 30 km.) Although the overall width of the stratiform region was nearly the same as that at CP-4, the intensity of the surface stratiform rainfall was at least 5 dB weaker (approximately a factor of 2 in rain rate). This weakening may have been a result of the rear inflow jet penetrating downward through the stratiform region at generally a greater height in this cross section compared to CP-4, therefore leading to more complete evaporation. At CP-3, the rear inflow stayed above the 0°C level, hence leading to the sublimation of slowly falling ice particles (Fig. 7b). At CP-4, the rear inflow was situated mainly below the 0°C level (in the area of most intense stratiform rain) and therefore the hydrometeors, which are of course raindrops, spent less time in the rear inflow layer because of their larger fallspeeds (Fig. 6b).

5. Vertically pointing data

Immediately after the passage of the convective line at CP-4 (0232 UTC), this radar was placed into the vertically pointing mode for a period of 60 min. One purpose of collecting data in this mode was to determine the presence of convective-scale variations in the

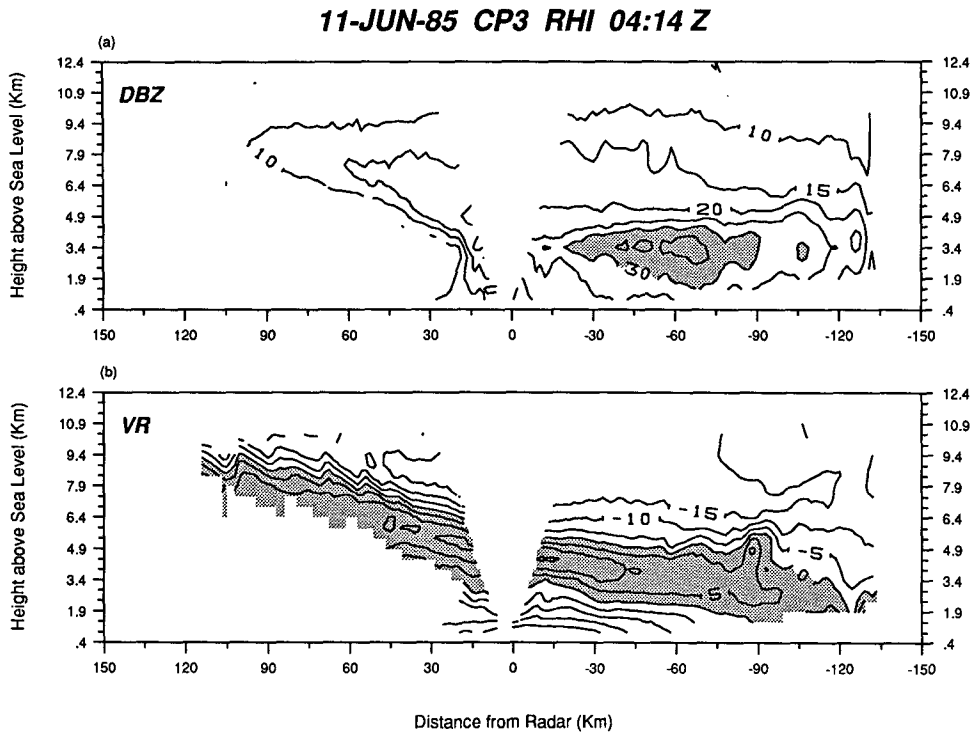

FIG. 7. As in Fig. 4 except for 0414 UTC at CP-3. (a) Reflectivity in dBZ; (b) horizontal relative flow in m s^{-1}.

stratiform region that might result from generating cells, which are usually present in other precipitating stratiform cloud systems (Hobbs and Locatelli 1978).

The resulting time–height cross sections of reflectivity (dBZ) and Doppler velocity (W) are shown in Figs. 8a, b. The time–height section of reflectivity from CP-4 (Fig. 8a) was obtained by averaging Z for all beams taken in a 2-min period and then contouring the resultant profiles. The horizontal resolution of the data thus becomes 1.45 km. Vertical resolution (150 m) is equivalent to the radar gate spacing. The Doppler velocity (W) has the same horizontal and vertical resolution. The back edge of the convective line is seen at the left-hand side of the plot, where the reflectivity is a maximum at all levels. This is followed by a transition zone, similar to that described by Smull and Houze (1985), in which the reflectivity is a minimum at middle and low levels. Immediately to the rear of the transition zone, the stratiform echo is clearly indicated by the bright band at approximately 3.6 km MSL associated with ice particle melting below the 0°C isotherm (3.9 km MSL). The reflectivity contours aloft are fairly flat, except for the relatively large tilting seen just behind the convective line. The tilting of the reflectivity contours in this region was likely a result of the fallout of higher density ice particles produced in the convective cells (see Fig. 9 and associated discussion in Rutledge and Houze 1987).

The time series of Doppler velocity (W) is the sum of the vertical air motion and particle fallspeed. Positive velocities indicate regions where updrafts were so strong that upward air motions locally overbalanced particle fallspeeds. Several such features are seen at upper levels just behind the convective region. The updrafts were probably remnants of convective updrafts carried into the stratiform region by the front-to-rear flow. The convective nature of the vertical motion pattern diminished in the stratiform region (for times later than 0300 UTC), probably as a result of the weakening of the small convective-scale updrafts with distance behind their source (i.e., the convective region). No pronounced or pervasive generative cell structure in the stratiform region was detected at the horizontal resolution obtained.

Regions where $W < 0$ may indicate downdrafts, or measure particle fallspeeds in regions of weak upward air motion. Convective scale downdrafts were present at the extreme left of the cross section between heights of 9 and 11 km. Maximum values of $\bar{W}$ were -8 m s^{-1}. This strong downward motion cannot be explained by particle fallspeeds, hence it represents convective-scale downdrafts. Upper-level convective-scale downdrafts in the vicinity of convective cells in squall lines were also noted by Heymsfield and Schotz (1985) and Smull and Houze (1987a). At lower levels a rather broad zone of large negative $\bar{W}$ values is found above

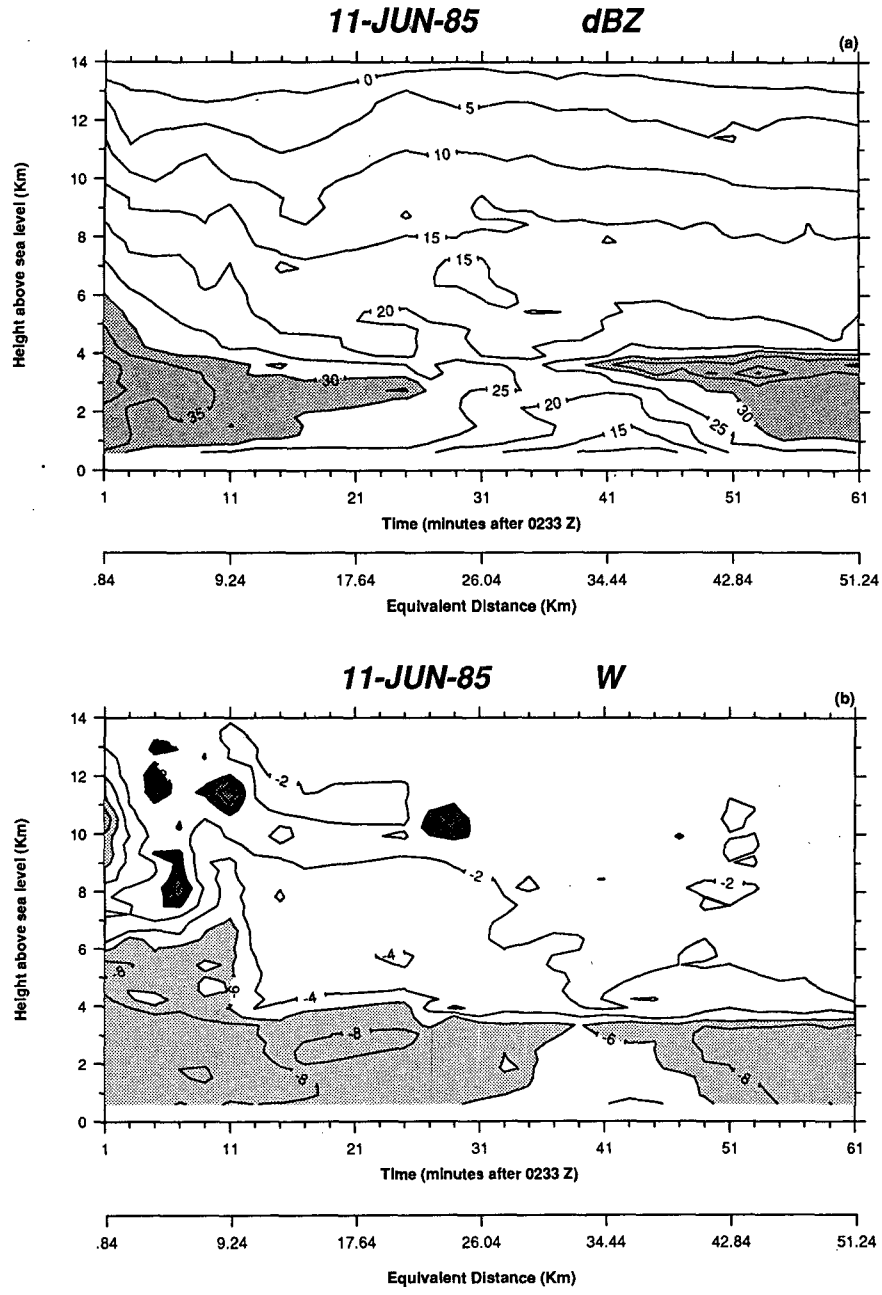

FIG. 8. Time–height sections from vertically pointing data at CP-4 for the period 0232–0332 UTC. (a) Reflectivity in dBZ. Shading denotes reflectivities > 30 dBZ. (b) Doppler velocities in m s^{-1} at vertical incidence. Light shading denotes Doppler velocities < −6 m s^{-1}. Heavy shading denotes velocities > 0. For velocities > 0, a 1 m s^{-1} contour interval is used.

the melting layer at distances up to 20 km behind the convective line. These values may be attributable to the fallout of large, relatively dense ice particles, or reflect the presence of a broad downdraft. [Our forthcoming dual-Doppler analyses indicate that this region contained a rather broad and intense (1–2 m s^{-1}) downdraft.] In situ airborne observations were not available this close to the convective line to allow for the determination of particle type and therefore terminal velocity.

Below the melting level, raindrop fallspeeds of 8–9 m s^{-1} were present (we assume the vertical air velocity is small compared to terminal velocities for raindrops, hence the Doppler velocity represents terminal fallspeed). These values are very similar to those deduced by Srivastava et al. (1986) for an Illinois squall line. As

those authors noted, such fallspeeds are rather large for a stratiform bright band situation. Fallspeeds of these magnitudes at 1013 mb correspond to drop diameters of 3–4 mm, which are near the maximum of observed raindrop size (Pruppacher and Klett 1978). Such large drops are not usually observed in extratropical cyclonic stratiform rainfall with precipitation rates similar to those here, ≤ 10 mm h^{-1}. We believe the drops in this case resulted from the melting of large ice particles produced in the convective cells that then formed aggregates just above the bright band. Fallspeeds below the melting level were weaker in the transition zone, in association with weaker echo and smaller precipitation rates.

6. Results of the EVAD analysis

Vertical profiles of horizontal wind, divergence, vertical air velocity, and particle terminal fallspeed can be obtained through the analysis of Doppler data collected by the three-dimensional conical scans using the EVAD (Extended Velocity–Azimuth Display) method (Srivastava et al. 1986; hereafter referred to as SML). The EVAD method of SML extends Browning and Wexler's (1968) VAD (Velocity–Azimuth Display) technique by using scans at various elevations to determine the particle fallspeed simultaneously with the wind and divergence. Browning and Wexler had to assume a fallspeed or determine it independently of the Doppler velocity measurements.

The EVAD method can be applied in regions where the horizontal and temporal variations of the fallspeed and horizontal divergence are small. This condition is usually satisfied in stratiform precipitation areas. Browning and Wexler (1968) noted that from data taken at a sequence of elevation angles, under these conditions, the wind component normal to the surface at a cylinder of some fixed radius (20 km in our case) can be determined on the boundary of the cylinder at a series of heights. At a given height, the wind components around the perimeter of the cylinder estimate the horizontal wind vector at the center of the cylinder and the mean divergence within the circular boundary. From the vertical profile of divergence, the vertical air motion was calculated by integration of the anelastic continuity equation. The divergence and vertical air velocity profiles were variationally adjusted (O'Brien 1970) so that the vertical velocity satisfied boundary conditions of zero at the ground and at the top of the echo.

Eight sets of EVAD scans were analyzed, four each from CP-3 and CP-4. Profiles of horizontal wind speed and direction, reflectivity, divergence, vertical motion and terminal fallspeed for one of those scans are shown in Fig. 9. These data were obtained during 0326–0334 UTC at CP-3, corresponding to the time at which the most intense portion of the trailing stratiform precipitation was over CP-3 (Fig. 10).

The vertical profile of relative horizontal wind normal to the length of the squall line (Fig. 9) exhibits three basic flow levels that are very consistent with the horizontal flow patterns shown in section 4 (see for example Fig. 7b). The storm-relative wind profile was obtained by using a storm speed of 14 m s^{-1} from 300°. Near the surface, strong easterly (front-to-rear) flow toward the rear edge of the stratiform region was present. Above this level, inflow into the storm from the rear was observed within maximum wind speed of approximately 10 m s^{-1}. The depth of the rear inflow was 3 km at this time. Above the rear inflow layer, strong front-to-rear flow was observed. The observed speeds, rear inflow depth and the height of the interface between the rear-to-front and front-to-rear flows agree well with findings described in section 4.

The reflectivity profile in Fig. 9 is typical of stratiform precipitation. The weak vertical gradient of reflectivity above the melting level is indicative of relatively slow particle growth probably attributable to depositional growth (Weiss and Hobbs 1975; Rutledge and Houze 1987). A distinct reflectivity maximum was present near 3.6 km resulting from ice particle melting which commenced at 3.9 km MSL.

The divergence profile (Fig. 9b) is characterized by alternating layers of divergence and convergence throughout the depth of the EVAD volume. Below 2 km the horizontal wind field was strongly divergent. A layer of convergence was located above, between 2 to 7 km MSL, with a strong peak of convergence at 4.8 km. The 0°C level at 3.9 km MSL was within this convergent layer, but below the level of maximum convergence. Between 7 and 11 km, divergence and convergence were rather weak. The layer between 11 and 14.5 km was characterized by moderate divergence.

The vertical air velocity is also shown in Fig. 9b. The vertical velocity profile is characterized by mesoscale subsidence below the 5.5 km level and mesoscale upward motion above this level. The subsidence motion began more than 1 km above the 0°C level and continued to the surface (~0.5 km MSL), but was notably most intense at the melting level.

The average terminal fallspeed for this EVAD analysis is also shown in Fig. 9b. This profile indicates fallspeeds from 1–2 m s^{-1} in the ice above the 0°C level with a sharp transition through the melting level to fallspeeds near 7 m s^{-1} in the rain below. This sharp increase in terminal fallspeeds at the 0°C level is probably associated with the presence of large aggregates above the 0°C level, which have rather low fallspeeds despite their large size, and the resultant formation of large drops with large fallspeeds below the 0°C level. Our values are also consistent with the terminal fallspeed profile obtained by SML (their Fig. 7).

Profiles of horizontal wind, reflectivity, divergence, vertical motion and terminal fallspeed for the EVAD volume acquired between 0345–0354 UTC at CP-4 are shown in Figs. 11a, b. As indicated by Fig. 12, this

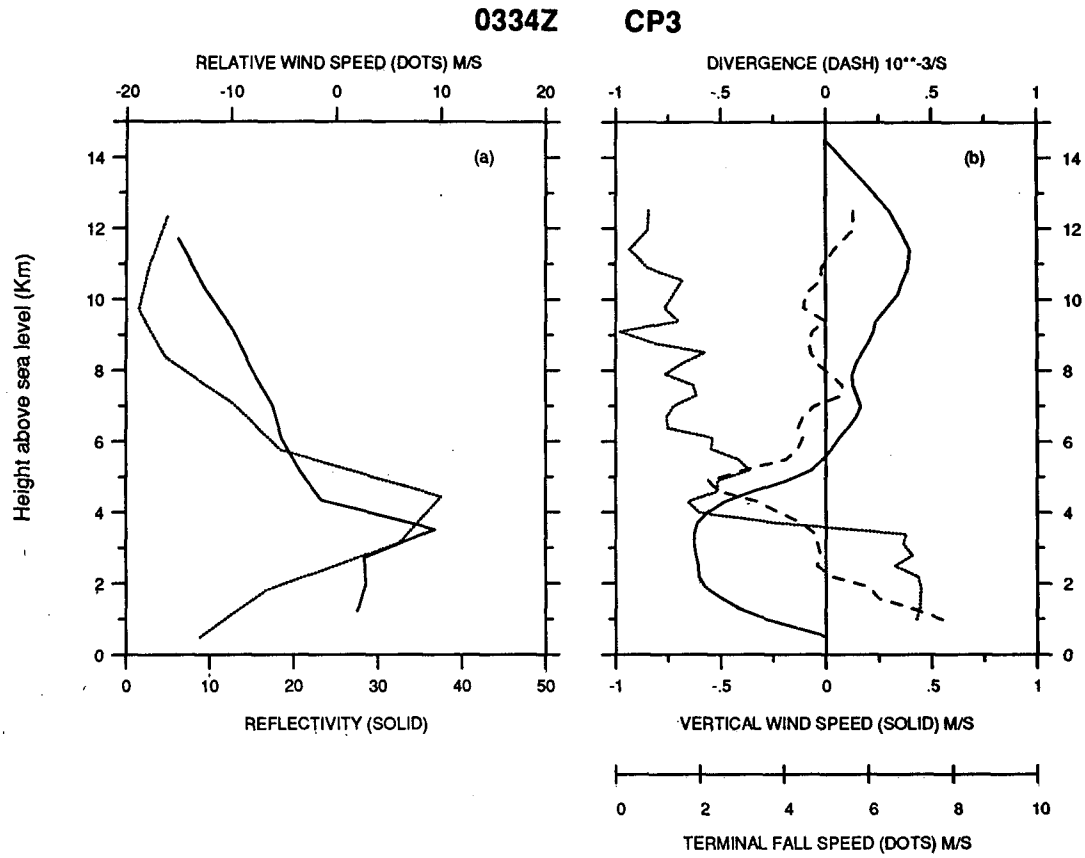

FIG. 9. Profiles derived from EVAD analysis at CP-3 from the volume beginning at 0334 UTC. (a) Reflectivity in dBZ (solid) and relative wind speed (dots) in the direction of squall line motion (m s^{-1}). (b) Divergence (dashed), terminal fallspeed (dots), and vertical air velocity (solid).

EVAD volume was located within the leading portion of the intense stratiform precipitation region in a similar position to the EVAD volume from CP-3 just 20 minutes earlier (cf. Fig. 10). To the extent the system was in a steady state during the twenty-minute period between scans, comparison of the profiles from CP-3 and CP-4 indicate variability in the along-line direction.

Profiles of relative horizontal wind speed and reflectivity from CP-4 are shown in Fig. 11a. These profiles are fairly similar to those at CP-3 (Fig. 9a) in shape, but important differences are found in magnitude. The rear inflow (again defined as the region in which the wind speed was >0) was similar in depth to that at CP-3 but weaker. Maximum speeds were 5 m s^{-1}, compared to 10 m s^{-1} at CP-3. Also, the rear inflow was lower in altitude at CP-4 and approximately 1 km shallower in overall depth. The top of the rear inflow was at 4 km MSL above CP-4, compared to 5 km MSL above CP-3. Hence, the rear inflow layer was confined more closely to the surface at CP-4 than at CP-3. This result is consistent with the vertical cross sections and with the weaker stratiform rainfall rates over CP-3, resulting from more intense evaporation (section 4).

The divergence profile above CP-4 is shown in Fig. 11b. The most intense portions of the profile again are

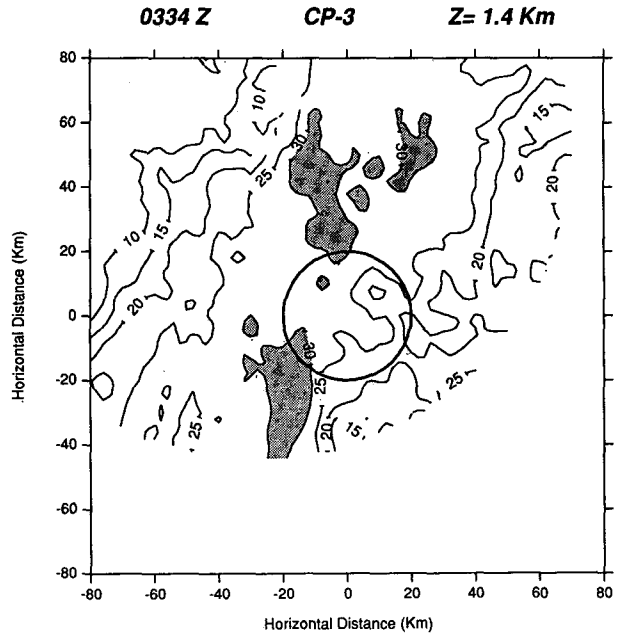

FIG. 10. Reflectivity (dBZ) from CP-3 at z = 1.4 km MSL for 0334 UTC. The circle of 20 km radius denotes the location of the imaginary EVAD circle. Reflectivities > 30 dBZ are indicated by the shading.

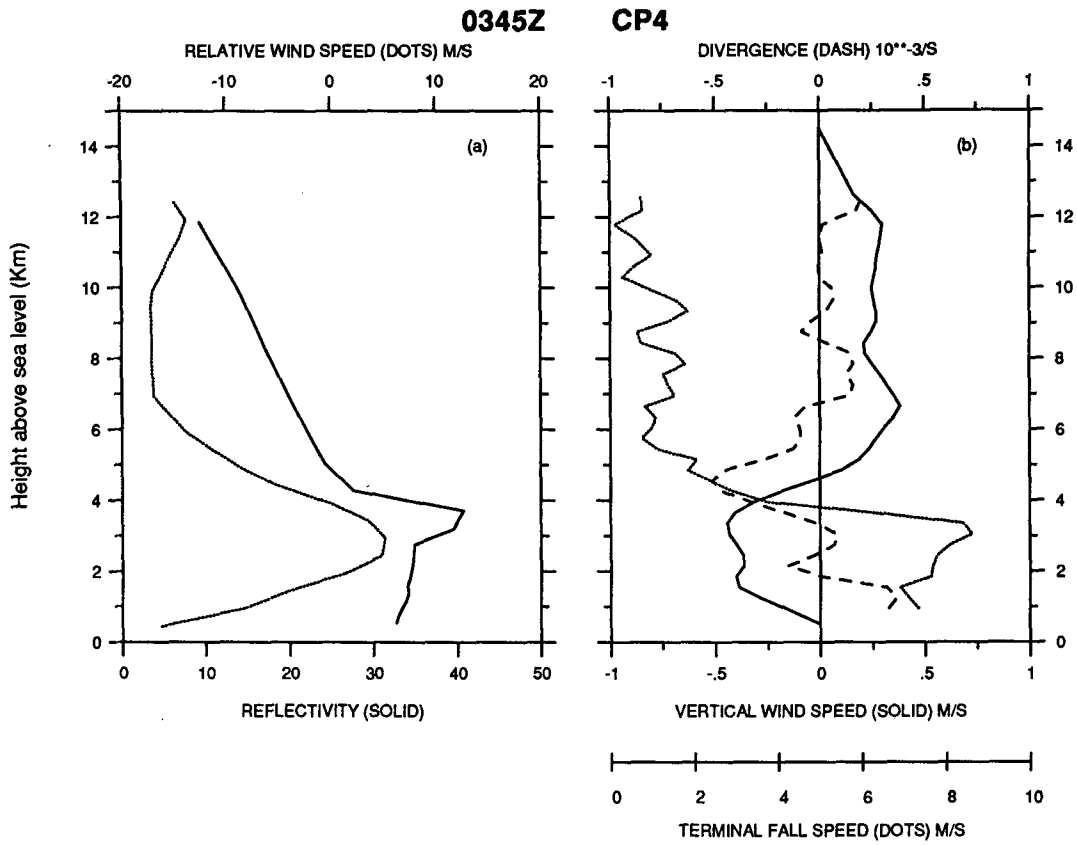

FIG. 11. Profiles derived from EVAD analysis at CP-4 from the volume beginning at 0345 UTC. (a) Reflectivity and relative wind speed as in Fig. 9. (b) Divergence, fallspeed and vertical air velocity as in Fig. 9.

seen in low-level divergence and deep midlevel convergence. Thus, this profile is similar to the divergence profile over CP-3 (cf. Fig. 9b). The midlevel convergence is similar in magnitude in both profiles ($\sim$5.5 $\times 10^{-4}$ s^{-1}) but dissimilar in altitude. Both convergence maximums occur precisely at the level where rear-to-front flow becomes front-to-rear flow (cf. Figs. 9a and 11a). Both profiles indicate weak upper-level divergence. The vertical motion pattern diagnosed over CP-4 shows a well-defined mesoscale updraft and downdraft. Differences between CP-3 and CP-4 are noted in the magnitude of the profiles and in the level separating mesoscale downward motion below from mesoscale upward motion above. The mesoscale downdraft is weaker and less vertically extensive over CP-4. We attribute this difference to the deeper and more intense rear inflow at CP-3, where the cooling resulting from evaporation was likely stronger.

The importance of melting and evaporation on the establishment of the mesoscale downdraft has been previously noted by Brown (1979) and Leary and Houze (1979). The maximum value of the mesoscale downdraft in both the CP-3 and CP-4 profiles occurs very close to the melting level ($\sim$3.9 km MSL). The level separating mesoscale downward motion from mesoscale upward motion in both profiles occurs es-

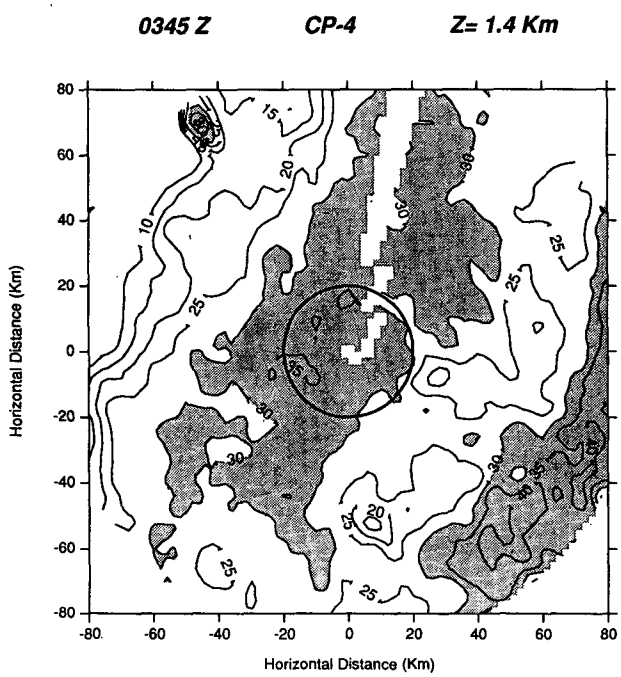

FIG. 12. Reflectivity (dBZ) from CP-4 at z = 1.4 km MSL for 0345 UTC. The circle denotes the location of the imaginary EVAD circle. Reflectivities > 30 dBZ are indicated by the shading.

sentially at the interface between rear-to-front and front-to-rear flow, which strongly suggests the rear inflow and the resultant drying is important to the establishment of a mesoscale downdraft. The mesoscale updraft over CP-4 was quite deep, with values in excess of 20 cm s^{-1} extending over a 7 km deep layer. The peak updraft of 40 cm s^{-1} was found at 6 km MSL. The profile over CP-3 is quite different, with the maximum updraft of 40 cm s^{-1} situated at the 11.5 km level.

The profile of terminal fallspeed at CP-4 (Fig. 11b) is similar to that at CP-3 (Fig. 9b); however, somewhat larger raindrop fallspeeds were found at CP-4, nearly 9 m s^{-1} compared to 7 m s^{-1} at CP-3. This finding is consistent with the occurrence of larger precipitation rates at CP-4 (section 4).

A time–height plot constructed from the four EVAD scans taken at CP-3 is shown in Fig. 13. In the time–height plot of divergence (Fig. 13a), the alternating layers of divergence and convergence seen in Fig. 9b can be identified. After 0322 UTC, the horizontal wind in the lowest levels became convergent, in agreement with the profile discussed by SML. While the very lowest levels become convergent toward the back of the stratiform region, the low-level divergent layer deepened with time and became less intense. Meanwhile, the midlevel convergent layer decreased in thickness and increased in intensity. The upper-level divergent layer, at 8 km MSL and above, persisted throughout the time period but weakened somewhat and shifted upward with time.

In conjunction with the divergence profile in Fig. 13a, the depth of the mesoscale downdraft decreased with time (Fig. 13b) but increased in intensity. The top of the mesoscale downdraft tilted upward with time, in direct relation to the position of the top of the rear inflow jet (cf. Fig. 7). This reinforces our earlier discussion and indicates the mesoscale downdraft commences at the interface between rear-to-front and front-to-rear relative flow. The most intense portion of the mesoscale downdraft was positioned near the melting level at earlier times (as indicated by the strong fallspeed gradient in Fig. 13c), indicating that melting may have played an important role in enhancing the strength of the mesoscale downdraft. At later times, however, the mesoscale downdraft was more intense, and the peak downdrafts were positioned well above the 0°C level. Apparently the downdraft was linked to cooling associated with sublimation in this region. The cooling resulting from the intrusion of the rear inflow was most pronounced along the rear of the system where the flow was the driest. The rear inflow must have become more moist as it intruded into the interior of the storm, since hydrometeors were evaporating into it. The mesoscale updraft was also well defined, with a depth > 8 km. Typical updraft values were 25 cm s^{-1} and the altitude of the maximum mesoscale updraft increased from 8 to 11 km during the period of observation and

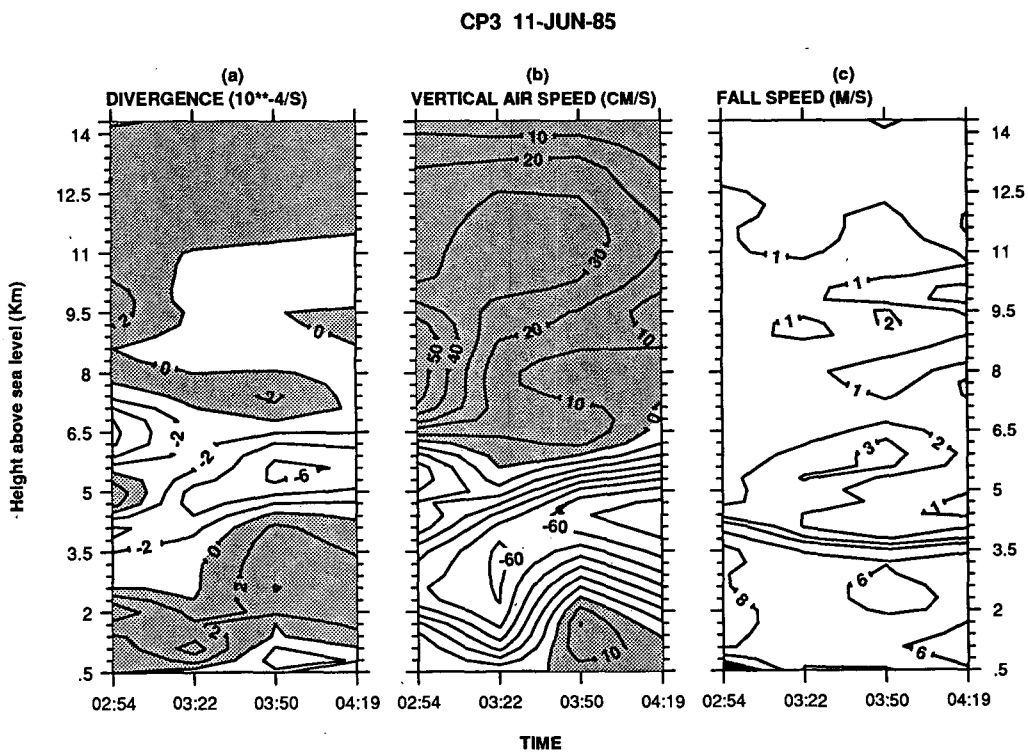

FIG. 13. Composite cross sections of EVAD derived values from CP-3. (a) Divergence (>0) and convergence (<0). Divergence is shaded. Units are 10^{-4} s^{-1}. (b) Vertical air velocity in cm s^{-1}. Upward motion is shaded. Contour interval is 10 cm s^{-1}. (c) Particle fallspeed in m s^{-1}.

decreased in value from 50 cm s^{-1} to less than 30 cm s^{-1}, consistent with the divergent layer aloft weakening and shifting upward. The shallow layer of upward motion at the surface at later times is similar to that detected by SML. This feature is apparently linked to convergence into the wake low pressure area observed by Johnson and Hamilton (1988).

The time–height section of particle terminal fallspeed (Fig. 13c) shows that the mesoscale updraft above ~6 km contained particles with fallspeeds on the order of 1 m s^{-1}. Slightly larger terminal fallspeeds, up to 2 m s^{-1}, between 4 and 6 km, indicate that particles there were generally large aggregates. However, the values of 3 m s^{-1} observed at 0350 UTC cannot be attributed to aggregates. These fallspeeds suggest the presence of other higher density ice particles such as graupel, possibly carried in from the convective line by the front-to-rear flow or generated in the stratiform region. The latter condition requires the presence of supercooled liquid water in this region. Although airborne measurements detected no liquid water above the 0°C level, the measurements were not extensive enough to rule out completely the presence of liquid water. It appears possible that the mesoscale updraft magnitudes observed in this case may have led to the presence of modest amounts of supercooled water, allowing graupel to form in the stratiform region. The considerable gradient in the terminal fallspeed with time, especially below the melting layer, with smaller fallspeeds associated with later times is consistent with decreasing precipitation rates observed at CP-3 (section 4).

The time–height cross sections derived from the four EVAD analyses at CP-4 are shown in Fig. 14. Although the profile of divergence obtained above CP-4 (Fig. 14a) was qualitatively similar to that obtained above CP-3, important differences were observed. First, the convergence at the lowest levels was not as pronounced in the portion of the storm that passed over CP-4 as it was in the northernmost portion of the storm that passed over CP-3. Secondly, the lower-level divergent layer was not observed to deepen with time over CP-4 as it did above CP-3 (although the intensity did decrease with time above both radar sites). Furthermore, the depth of the midlevel convergence remained fairly constant above CP-4 and the intensity of the midlevel convergence was not observed to increase with time as it did above CP-3. Finally, the upper-level divergent layer above CP-4 did not decrease in depth as it appeared to do above CP-3.

As a result of the differences in divergence observed above each radar site, the mesoscale downdraft over CP-4 (Fig. 14b) was diagnosed as being weaker and shallower than at CP-3. Furthermore, the mesoscale downdraft above CP-4 weakened with time in contrast to the strengthening with time observed further north at the CP-3 location. The mesoscale updraft was deeper above CP-4 and increased in strength throughout most of the analysis time. The time–height section of ter-

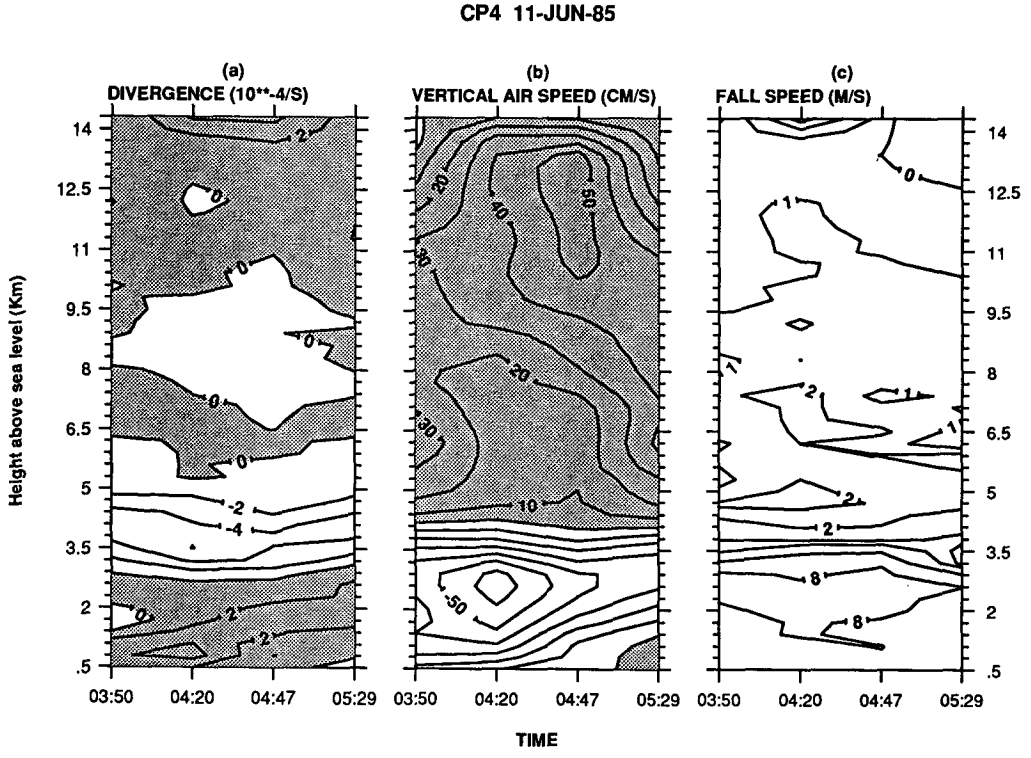

FIG. 14. Composite cross sections of EVAD derived values from CP-4. (a) Divergence (>0) and convergence (<0) as in Fig. 13. (b) Vertical air velocity in cm s^{-1} as in Fig. 13. (c) Particle fallspeed in m s^{-1}.

minal fallspeed over CP-4 (Fig. 14c) indicates that fallspeeds below the 0°C level were greater than those over CP-3, consistent with the higher precipitation rates at CP-4.

The absence of strong low-level convergence and rising motion at the rear of the stratiform region in the CP-4 cross section is consistent with the work of Johnson and Hamilton (1988), who found the strongest wake low area near CP-3. A weaker wake low feature was observed near CP-4. As they discussed, the wake low is evidently a surface manifestation of the rear inflow jet, and the subsidence warming generated by it. The subsidence warming then generates pressure falls, followed by low-level convergence and rising motion at the surface. Our EVAD cross sections support their argument. Both stronger rear inflow and more intense downward motion occurs at CP-3 compared to CP-4, which apparently led to surface pressure falls, convergence and rising motion at the surface. The weaker rear inflow at CP-4 resulted in weaker subsidence, less warming and hence weaker upward motion.

7. Comparison of vertical motion profiles with other studies

Although we must be cautious about generalizing from the results of the vertical motion profiles in Figs. 9b and 11b (clearly variability among vertical motion profiles exists within this system alone), it is nonetheless interesting to compare our profiles with profiles of vertical motion obtained in the trailing stratiform regions of other squall lines. Mesoscale vertical motions in midlatitude systems have been determined previously by SML, Ogura and Liou (1980), and Smull and Houze (1987a). For tropical systems, profiles of vertical motion have been discussed by Gamache and Houze (1982, 1985), Johnson (1982), Houze and Rappaport (1984), Chong et al. (1987), and Balsley et al. (1988). The study of Chong et al. was continental tropical; it was of a West African squall line observed during COPT 81. The other tropical profiles were obtained in oceanic cloud systems. Here we compare our results in some detail to the results of SML and Chong et al. since they used high-resolution single-Doppler radar VAD analysis similar to ours to obtain the vertical profiles. The other studies employed other technologies and analysis techniques that affect the resolution and detail of the resulting w profiles. Our comparison with profiles discussed in these latter studies will be limited to the overall shape of the profile and the heights at which the most intense upward and downward motions are situated. Houze (1987) presents a more complete discussion of the vertical motion profiles obtained by all the methods.

In comparing our w profiles to profiles computed by SML and Chong et al., we have chosen to compare mean vertical motion profiles from our four individual profiles at each radar with a mean w profile computed from the Chong et al. data (a total of three profiles were used from their study: profiles 3, 4, and 5). These are compared with the SML profile, which consists of a single analysis time only.

These resultant profiles are shown in Fig. 15. All profiles show a well-defined mesoscale updraft and downdraft. The peak mesoscale updraft values are all between 30–40 cm s^{-1}. The location of the maximum upward motion in each of the profiles is very similar for the SML (Illinois) and the 10–11 June storm (~11 km MSL), but occurs markedly lower for the West African case (~7 km MSL). Interestingly, the peaks in the upward motion profiles in Gamache and Houze (1982), Johnson (1982), and Houze and Rappaport (1984) all occur very near to 11 km MSL. These are all oceanic tropical cases for which rawinsonde data were used to deduce the vertical motion. The magnitudes of the vertical motions were considerably smaller than that found here, possibly as a result of the lower resolution of the sounding data. The West African system was considerably shallower than the midlatitude U.S. cases (both the convective cells and stratiform echo tops were lower). This fact may explain the lower height of the peak mesoscale updraft in that case.

The magnitudes of the diagnosed mesoscale downdrafts show more variability than the mesoscale updrafts. Peak downdraft speeds range from −20 to nearly −60 cm s^{-1}. The mesoscale downdraft begins near the melting level for all profiles with the exception of that at CP-3, where it commenced some 2 km higher. This profile also exhibits a peak downdraft value near the melting level, whereas the maximum downdraft speeds in the other profiles occurred about 1.5 km below the melting level. The mesoscale downdraft at CP-3 was

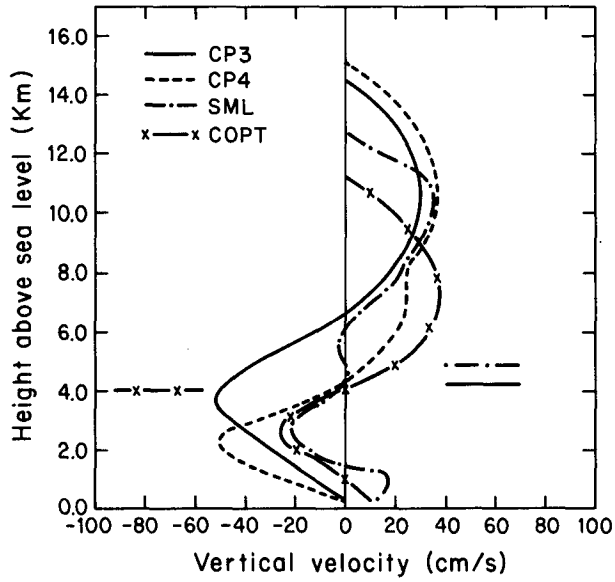

FIG. 15. Profiles of vertical velocity derived from single-Doppler data. See text for details. The horizontal lines indicate the 0°C level for the various cases. The solid horizontal line represents the 0°C level at both CP-3 and CP-4.

apparently initiated by cooling as a result of sublimation and enhanced by cooling associated with melting. The CP-3 downdraft profile appears to have been related to the topography of the rear inflow. The rear inflow above this radar was considerably deeper and extended to a greater height compared to the other three cases.

Evidence from these four cases (considering the CP-3 and CP-4 cases as separate events) shows that the strength of the mesoscale downdraft is correlated with the rear inflow intensity in a positive way. The most intense rear inflow ($\sim$15 m s^{-1}) occurred in the CP-3 case (strongest mesoscale downdraft). Rear inflow speeds at CP-4 peaked at 10 m s^{-1}, at 5 m s^{-1} for the SML case, and were small or zero for the West African case (for their profiles 3, 4, and 5). The rear inflow jet is important in the supply of drier air into the storm interior which is important to hydrometeor evaporation resulting in cooling and the generation of a mesoscale downdraft. Evidently this process is enhanced with stronger rear inflow. More cases should be examined to test the generality of this observation.

8. Conclusions

The 10–11 June PRE-STORM squall line began as an intense line of convective showers oriented along a northeast–southwest line. Approximately 3.5 h elapsed between the time of initial convective development until the appearance of a radar bright band in a trailing stratiform region. We attribute this first appearance of the bright band to the arrival of ice particles at the 0°C level that were injected into the upper troposphere by the deep convective cells. Some three more hours elapsed before the stratiform region reached maturity. At about the time the radar bright band was first observed within the evolving stratiform region, the storm's cloud shield had achieved the size criteria to be classified as an MCC (Maddox 1980).

The kinematic structure of the horizontal flow in the 10–11 June storm was found to be similar to that of previously analyzed midlatitude squall line storms. However, as a result of extensive Doppler radar observations (both in time and space), further details of the horizontal flow have been revealed. Strong rear inflow was present throughout the analysis period, which spanned nearly 4 h. It was observed to acquire a sharper tilt as it passed into the convective region of the storm, probably as a result of colliding with convective downdrafts. Rear inflow existed prior to the development of a broad trailing stratiform region, in contrast to the case described by Smull and Houze (1985, 1987b). For a rather similar squall line in Oklahoma, they found rear inflow only late in the storm's lifetime.

Comparisons of the rear inflow structure observed by the NCAR CP-3 and CP-4 radars revealed considerable variability in intensity, depth and tilt of the rear inflow jet within the trailing stratiform region. At CP-3, located 60 km north-northwest of CP-4, the inflow entered the storm from the rear at nearly 10 km MSL in altitude. The top of the rear inflow remained above the melting level as it penetrated downward through the storm, finally dropping completely below the melting level near the convective line. At CP-4 the rear inflow entered the storm at a slightly lower altitude, and dropped completely below the 0°C level farther to the rear of the convective line than at CP-3.

The strongest convergence in the stratiform region was consistently located along the tilted interface between the rear inflow and front-to-rear flow aloft. Divergence was generally present below this layer with the exception of the region immediately to the rear of the surface stratiform rain, where convergence was present. Apparently this convergence was associated with a strong wake-low feature (Johnson and Hamilton 1988). Weak upward motion in the vicinity of this low evidently produced several shallow convective cells along the rear of the stratiform precipitation zone.

Extensive measurements of the mesoscale vertical motion pattern were obtained within the trailing stratiform region by the EVAD technique. A well-defined mesoscale updraft and downdraft were evident in all profiles (eight total). The base of the mesoscale downdraft was consistently situated near the top of the rear inflow jet, suggesting sublimation or evaporation (depending on whether the top of the rear inflow was situated above or below the melting level) was important in generating the mesoscale subsidence. As the rear inflow sloped upward with height toward the rear of the storm, so the mesoscale downdraft deepened with distance behind the convective line. A clear linkage is evident between the rear inflow and mesoscale downdraft. Comparisons between our observations and other similar cases suggests that the strength and dryness of the rear inflow determines the intensity of the mesoscale downdraft.

The transition zone and a portion of the stratiform region behind the convective line were observed with one Doppler radar fixed at vertical incidence. The resulting data show that convective-scale updrafts and downdrafts (1 to 6 m s^{-1}) were embedded in this region at upper levels, within a 20 km wide zone behind the convective line. The updraft structure took on a stratiform nature for distances greater than 20 km behind the convective line as no embedded convective-scale features were observed.

Because of the comprehensive radar sampling in this case, the kinematic and microphysical structure of a squall line with trailing stratiform precipitation has been more completely documented than previously. Models and theoretical studies are now challenged to account for such features as the appearance of the tilted mesoscale rear inflow jet, subsidence above the melting layer at the rear of the storm, and the subsequent enhancement of the subsidence by the melting layer toward the interior of the storm. Microphysical modeling studies must account for the particle fall velocity patterns deduced in this case. The present single-Doppler

analysis, moreover, is a solid foundation and background for more detailed studies of regions of the storm for which dual-Doppler analyses can be constructed. The dual-Doppler studies will provide three-dimensional fields of the horizontal wind vector and the vertical air motion. Ultimately, the Doppler-derived air motions can be used in detailed studies of the water, heat, momentum and vorticity budgets of this storm.

Acknowledgments. The CP-3 and CP-4 Doppler radars in PRE-STORM were supported by the National Science Foundation, the National Oceanic and Atmospheric Administration (NOAA) and the National Center for Atmospheric Research (NCAR); these radars were operated by NCAR staff. Analyses of the satellite and NWS radar data used in this study were provided to the authors by the NOAA Weather Research Program. The digitized NWS data were collected at ICT by the NOAA Hurricane Research Division and Texas Tech University. We also thank the many PRE-STORM scientists who participated in this field program. The authors have been supported in this work by the National Science Foundation under Grants ATM-8413546, ATM-8419543, ATM-8521403, ATM-8602411 and ATM-8608467.

REFERENCES

Balsley, B. B., W. L. Ecklund, D. A. Carter, A. C. Riddle and K. S. Gage, 1988: Average vertical motions in the tropical atmosphere observed by a radar wind profiler in Pohnpei. *J. Atmos. Sci.*, **45,** 396–405.

Brown, J. M., 1979: Mesoscale unsaturated downdrafts driven by rainfall evaporation. *J. Atmos. Sci.*, **36,** 313–338.

Browning, K. A., and R. Wexler, 1968: The determination of kinematic properties of a wind field using Doppler radar. *J. Appl. Meteor.*, **7,** 105–113.

Chong, M., P. Anayenc, G. Scialom and J. Testud, 1987: A tropical squall line observed during COPT '81 experiment in West Africa. Part I: Kinematic structure inferred from dual-Doppler radar data. *Mon. Wea. Rev.*, **115,** 670–694.

Cunning, J. B., 1986: The Oklahoma–Kansas Preliminary Regional Experiment for STORM-Central. *Bull. Amer. Meteor. Soc.*, **67,** 1478–1486.

Fujita, T. T., 1955: Results of detailed synoptic studies of squall lines. *Tellus*, **7,** 405–436.

Gamache, J. F., and R. A. Houze, Jr., 1982: Mesoscale air motions associated with a tropical squall line. *Mon. Wea. Rev.*, **110,** 118–135.

——, and ——, 1985: Further analysis of the composite wind and thermodynamic structure of the 12 September GATE squall line. *Mon. Wea. Rev.*, **113,** 1241–1259.

Hamilton, R. A., and J. W. Archbold, 1945: Meteorology of Nigeria and adjacent territory. *Quart. J. Roy. Meteor. Soc.*, **71,** 231–264.

Heymsfield, G. M., and S. Schotz, 1985: Structure and evolution of a severe squall line over Oklahoma. *Mon. Wea. Rev.*, **113,** 1563–1589.

Hobbs, P. V., and J. D. Locatelli, 1978: Rainbands, precipitation cores and generating cells in a cyclonic storm. *J. Atmos. Sci.*, **35,** 230–241.

Houze, R. A., Jr., 1987: Observed structure of Mesoscale Convective Systems and implications for large-scale heating. *Proc., ECMWF Workshop on Diabatic Forcing,* European Centre for Medium-Range Weather Forecasting, Reading (in press).

——, and E. N. Rappaport, 1984: Air motions and precipitation structure of an early summer squall line over the eastern tropical Atlantic. *J. Atmos. Sci.*, **41,** 553–574.

Johnson, R. H., 1982: Vertical motion in near-equatorial winter monsoon convection. *J. Meteor. Soc. Japan*, **60,** 682–690.

——, and P. J. Hamilton, 1988: The relationship of surface pressure features to the precipitation and air flow structure of an intense midlatitude squall line. *Mon. Wea. Rev.*, **116,** in press.

Kessinger, C. J., P. S. Ray and C. E. Hane, 1987: The 19 May 1977 Oklahoma squall line. Part I: A multiple Doppler analysis of convective and stratiform structure. *J. Atmos. Sci.*, **44,** 2840–2864.

Leary, C. A., and R. A. Houze, Jr., 1979: Melting and evaporation of hydrometeors in precipitation from anvil clouds of deep tropical convection. *J. Atmos. Sci.*, **36,** 689–679.

——, and E. N. Rappaport, 1987: The life cycle and internal structure of a mesoscale convective complex. *Mon. Wea. Rev.*, **115,** 1503–1527.

LeMone, M. A., 1983: Momentum transport by a line of cumulonimbus. *J. Atmos. Sci.*, **40,** 1815–1834.

Maddox, R. A., 1980: Mesoscale convective complexes. *Bull. Amer. Meteor. Soc.*, **61,** 1374–1387.

Mohr, C. G., L. J. Miller and R. L. Vaughan, 1979: An economical procedure for Cartesian interpolation and display of reflectivity factor data in three-dimensional space. *J. Appl. Meteor.*, **18,** 661–670.

Newton, C. W., 1950: Structures and mechanisms of the prefrontal squall line. *J. Meteor.*, **7,** 210–222.

O'Brien, J. J., 1970: Alternative solutions to the classical vertical velocity problem. *J. Appl. Meteor.*, **9,** 197–203.

Ogura, Y., and M. T. Liou, 1980: The structure of the midlatitude squall line: A case study. *J. Atmos. Sci.*, **37,** 553–567.

Pedgley, D. E., 1962: A meso-synoptic analysis of the thunderstorms of 28 August 1958. *Brit. Meteor. Off., Geophys. Memo.*, No. 106, 74 pp.

Pruppacher, H. R., and J. D. Klett, 1978: *Microphysics of Clouds and Precipitation.* Reidel, 714 pp.

Rutledge, S. A., and R. A. Houze, Jr., 1987: A diagnostic modeling study of the trailing stratiform region of a midlatitude squall line. *J. Atmos. Sci.*, **44,** 2640–2656.

Smull, B. F., and R. A. Houze, Jr., 1985: A midlatitude squall line with a trailing region of stratiform rain: Radar and satellite observations. *Mon. Wea. Rev.*, **113,** 117–133.

——, and ——, 1987a: Dual-Doppler radar analysis of a midlatitude squall line with a trailing region of stratiform rain. *J. Atmos. Sci.*, **44,** 2128–2148.

——, and ——, 1987b: Rear inflow in squall lines with trailing stratiform precipitation. *Mon. Wea. Rev.*, **115,** 2869–2889.

Srivastava, R. C., T. J. Matejka and T. J. Lorello, 1986: Doppler radar study of the trailing anvil region associated with a squall line. *J. Atmos. Sci.*, **43,** 356–377.

Weiss, R. R., and P. V. Hobbs, 1975: The use of vertically pointing pulsed Doppler radar in cloud physics and weather modification studies. *J. Appl. Meteor.*, **14,** 222–231.

Zipser, E. J., 1969: The role of organized unsaturated convective downdrafts in the structure and rapid decay of an equatorial disturbance. *J. Appl. Meteor.*, **8,** 799–814.

——, 1977: Mesoscale and convective-scale downdrafts as distinct components of squall-line structure. *Mon. Wea. Rev.*, **105,** 1568–1589.